

ARTICLE OPEN



Towards weathering and corrosion resistant, self-warning and self-healing epoxy coatings with tannic acid loaded nanocontainers

Jinke Wang^{1,2}, Weimin Tan³, Hao Yang^{1,2}, Xingxing Rao³, Xinliang Luo³, Lingwei Ma^{1,2,4✉}, Chenhao Ren^{1,2}, Arjan Mol⁵ and Dawei Zhang^{1,2,4✉}

In this work, an active protective epoxy coating with weathering resistant, corrosion-warning, and self-healing properties was developed by incorporating tannic acid (TA) loaded mesoporous silica (MSN-TA) nanocontainers. The introduction of MSN-TA nanocontainers could alleviate the coating degradation via scavenging the radicals generated during UV irradiation. Compared with the blank coating, the coating containing 5 wt.% MSN-TA nanocontainers exhibited much less degradation in surface morphology, wettability and glossiness, and maintained a good barrier property after 384 h of accelerated weathering. Once the coating was damaged, the released TA could react with the Fe^{3+} ions to form a chelate that endowed the coating scratch with a visible black coloration, i.e. triggering a self-warning capability to indicate the initial onset of corrosion. In addition, the generated chelate could inhibit extensive corrosion propagation, offering a significant self-healing effect demonstrated by the stabilized impedance modulus values during 28 days of immersion in NaCl solution.

npj Materials Degradation (2023)7:39; <https://doi.org/10.1038/s41529-023-00360-7>

INTRODUCTION

Natural organisms have evolved different tissue barriers to protect themselves in harsh environments and against mechanical attack, and also to respond autonomously to sense and heal damages. In contrast, common organic barrier coatings suffer severely when facing prolonged weathering conditions and aggressive environments or inevitable external mechanical damage^{1–3}. During the service life of organic coatings, photo radiation will cause the generation and continuous propagation of free radicals, leading to the rupture of polymeric chains that might weaken the physical barrier effect of the coating^{4,5}. The continuous ingress of corrosive media will result in corrosion and subsequent accumulation of corrosion products at the interface between metal and coating and also delamination of coatings^{6,7}. Moreover, intrinsically present and externally applied coating defects and cracks will accelerate the failure of organic coatings^{8–10}. Without accurate detection of coating damage and timely repairs, the metal substrate underneath the coating will experience progressive corrosion attack, which jeopardizes the structural integrity of coated metals^{11,12}. Therefore, enhancing the weathering resistance, as well as developing corrosion self-warning and self-healing properties are three important aspects to extend the service life of protective coatings and the underlying metal structures.

One of the most efficient approaches to strengthen the weathering resistance of organic coatings is the introduction of radical scavengers, such as hindered amines and hindered phenols^{13,14}. However, these synthetic radical scavengers often exhibit potential hazards to human health and environment¹⁵. Recently, a variety of environmentally friendly radical scavengers

have been introduced, including graphene¹⁶, carbon dots¹⁷, $\text{Ti}_3\text{C}_2\text{T}_x$ MXene¹⁸, and a series of bio-based additives, such as chitosan¹⁹, phytic acid²⁰, and plant polyphenols²¹. Tannic acid (TA) is considered as a promising green radical scavenger benefiting from its abundant o-phenylphenol groups, which can donate hydrogen atoms to the free radicals generated from the weathering conditions and thus stop the free-radical chain reactions²². Peng et al.²³ used TA and tung oil for the surface treatment of wood. Due to the significant radical scavenging property of TA and the barrier effect of tung oil, the surface deterioration of wood has been successfully alleviated during 960 h of accelerated weathering testing. Qiu et al.²⁴ synthesized a bio-based additive by combining the UV light absorption ability of melamine and the radical scavenging property of TA to protect polylactic acid (PLA) against UV degradation. The mass retention ratio of PLA with 5 wt.% additive was 88.8%, which was ~10% higher than that of the blank PLA sample after a 100 h UV aging test, indicating that TA is conducive to improving the weathering resistance of polymers.

Besides, the abundant o-phenylphenol groups of TA allow it to chelate with different metal ions and generate a variety of prominent colors²⁵. For instance, when TA molecules interact with Fe^{3+} ions, a black colored chelate compound will be rapidly formed. During the corrosion of steel, Fe^{2+} ions will be initially generated from the anodic site and then be oxidized into Fe^{3+} ions, informing that TA can be applied as an early corrosion self-warning color indicator for steel substrates²⁶. Moreover, the strong chelation effect of TA also makes it a high potential green corrosion inhibitor^{27,28}. The corrosion inhibition effect of TA is mainly attributed to the formation of ferric tannate layers on the steel surface. Qian et al.²⁷ studied the corrosion inhibition effect of

¹Beijing Advanced Innovation Center for Materials Genome Engineering, Institute for Advanced Materials and Technology, University of Science and Technology Beijing, Beijing 100083, PR China. ²National Materials Corrosion and Protection Data Center, University of Science and Technology Beijing, Beijing 100083, PR China. ³CNOOC Changzhou Paint and Coatings Industry Research Institute Limited Liability Company, Changzhou 213016 Jiangsu, PR China. ⁴BRI Southeast Asia Network for Corrosion and Protection (MOE), Shunde Graduate School of University of Science and Technology Beijing, Foshan 528399, PR China. ⁵Department of Materials Science and Engineering, Delft University of Technology, Delft, Netherlands. ✉email: mlw1215@ustb.edu.cn; dzhang@ustb.edu.cn

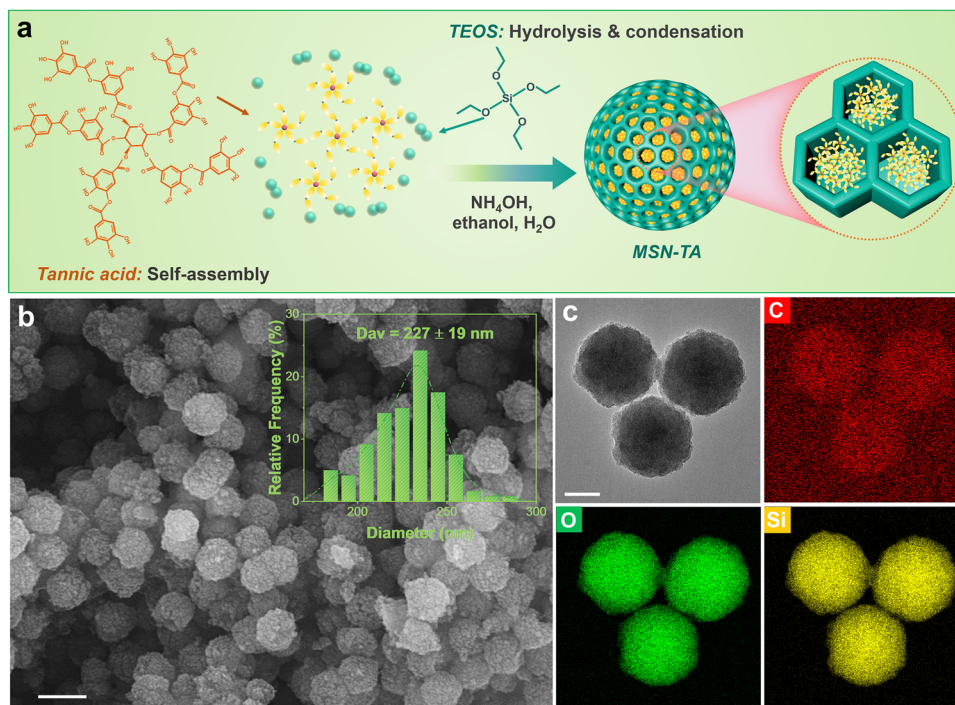


Fig. 1 The formation of MSN-TA nanocontainers and their morphologies. **a** The preparation schematic for MSN-TA nanocontainers; **b** SEM (scale bar: 300 nm) and **c** TEM images of MSN-TA nanocontainers, and the corresponding EDS element mapping results (scale bar: 100 nm).

TA against mild steel corrosion in seawater wet/dry cyclic condition. TA exhibited a high inhibition efficiency of ~86%, which could provide continuous and stable protection performance for the mild steel under these conditions. Benefiting from the good inhibition effect and its non-toxic property, TA has also been introduced into organic coatings to realize a timely self-healing function^{29,30}. Wu et al.²⁹ applied a TA layer onto carbonate (CaCO_3) microspheres loaded with benzotriazole (BTA) corrosion inhibitors, which were then incorporated into an epoxy matrix to establish a self-healing coating. When corrosion occurred at the damage area of the coating, TA and BTA molecules were simultaneously released and adsorbed on the exposed metal surface to suppress the corrosion process.

In this work, a composite coating with enhanced weathering resistance, as well as corrosion-warning and self-healing functions was developed via the introduction of TA-based nanocontainers in the coating. TA was encapsulated into mesoporous silica nanoparticles (MSN-TA) via hydrolysis and condensation of tetraethyl orthosilicate (TEOS) around a TA self-assembled template under alkaline conditions. On the one hand, the introduction of MSN-TA nanocontainers was beneficial to alleviating the weathering degradation of epoxy coating by scavenging the free radicals and preventing the invasion of aggressive media. On the other hand, when the coating was damaged, TA could release from the nanocontainers and react with the Fe^{3+} ions generated from the underneath steel surface to form a chelate compound. A prominent black-colored chelate adsorption layer was formed to offer the corrosion-warning and self-healing smart functions. The morphology and chemical composition of MSN-TA nanocontainers were characterized via scanning electron microscopy (SEM), transmission electron microscopy (TEM), Fourier transform infrared spectroscopy (FTIR), and thermogravimetric analysis (TGA). The weathering resistance of different coatings was evaluated by testing their surface morphology, wettability, glossiness, adhesion strength, and corrosion resistance during accelerated weathering experiments. The corrosion-warning capability of the coatings was recorded by digital images to reflect

their color changes. The corrosion resistance and self-healing performance of the coatings were evaluated using electrochemical impedance spectroscopy (EIS) and surface characterization.

RESULTS AND DISCUSSION

Preparation and characterization of MSN-TA nanocontainers

The preparation schematic of the MSN-TA nanocontainers is presented in Fig. 1a. Under alkaline conditions, the TA molecules were self-assembled as the porogen³¹, and the MSN shell was formed by hydrolysis and condensation of TEOS³². The morphology of as-prepared MSN-TA nanocontainers was characterized by SEM and TEM observations shown in Fig. 1b, c, displaying well-dispersed near-spherical nanoparticles and narrow size distribution with an average diameter of ~227 nm. The elemental distributions of MSN-TA nanocontainers were characterized by energy dispersive spectroscopy (EDS) mapping in Fig. 1c. The Si element mapping result outlined the structure of MSN. The EDS image of carbon element demonstrated the successful loading of TA. Meanwhile, the distribution of oxygen element can be attributed to both the mesoporous silica structure and the loaded TA molecules.

FTIR spectroscopy was conducted to confirm the chemical components of MSN-TA nanocontainers. The FTIR spectra of TA, MSN, and MSN-TA are shown in Fig. 2a. The peaks for the MSN-TA nanocontainers at 802 and 1080 cm^{-1} were assigned to the symmetric stretching and asymmetric vibration of Si-O-Si respectively, which originated from the mesoporous silica structure¹¹. The peaks at 1453 and 1613 cm^{-1} corresponded to the stretching vibrations of the aromatic ring from TA⁶. The peaks at 1710 and 3420 cm^{-1} were attributable to the stretching vibration of C=O and C-OH groups from TA, respectively³³. Figure 2b shows the N_2 adsorption-desorption isotherms of MSN-TA and the MSN control sample (obtained by calcining the MSN-TA nanocontainers to completely remove the inside TA molecules). The MSN-TA nanocontainers exhibited a very low adsorption amount of N_2 , with a Brunauer-Emmett-Teller (BET) surface area of 21.3 $\text{m}^2 \text{g}^{-1}$

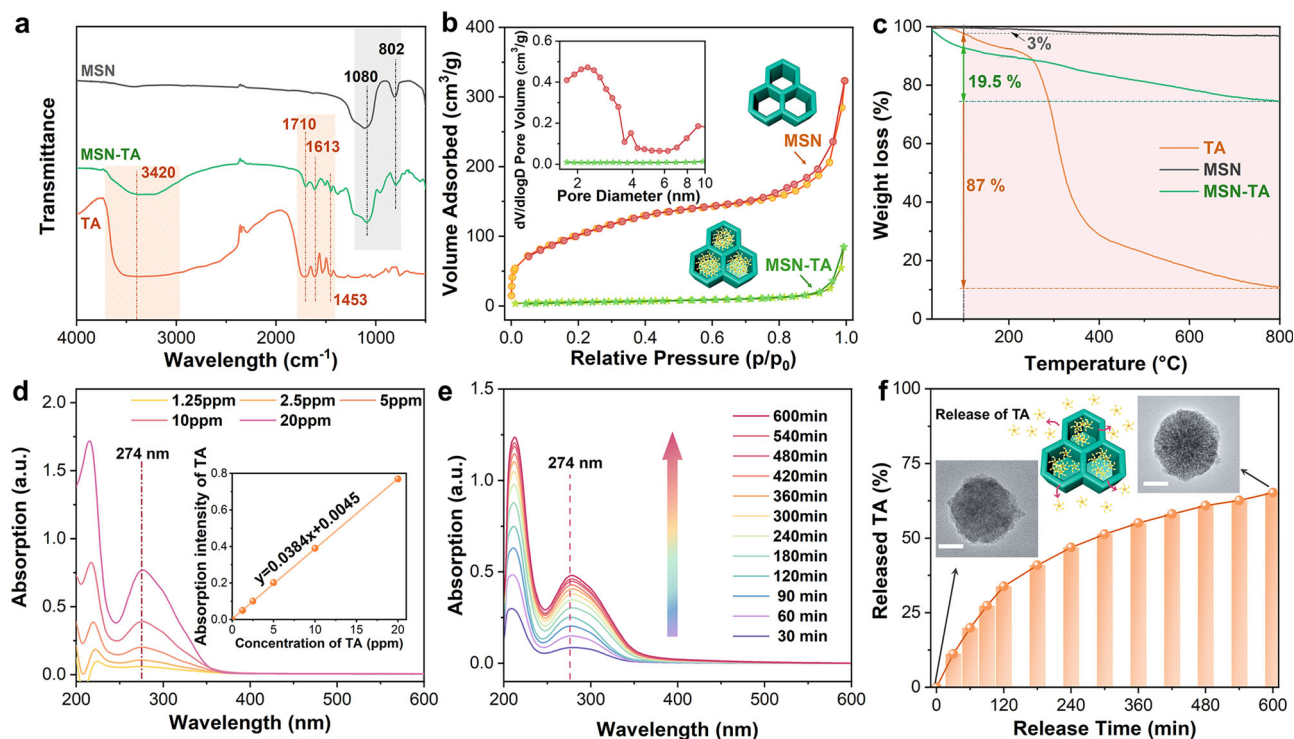


Fig. 2 The chemical components, mesoporous structure and release behavior of MSN-TA nanocontainers. **a** FTIR spectra of TA, MSN and MSN-TA nanocontainers; **b** N_2 adsorption-desorption isotherm and pore diameter distribution (inset) of MSN and MSN-TA; **c** TGA curves of TA, MSN and MSN-TA nanocontainers; **d** the UV-Vis spectra and the corresponding standard curves (inset) of TA in 3.5 wt.% NaCl solutions; **e** the UV-Vis spectra of TA released from MSN-TA nanocontainers in 3.5 wt.% NaCl solutions after different release time; **f** the release percentage of TA from MSN-TA in 3.5 wt.% NaCl solutions. The insets are the TEM images of MSN-TA nanocontainers before and after 600 min of release (scale bar: 100 nm).

and no obvious nanopores. After removing TA from MSN-TA nanocontainers by calcination, the N_2 adsorption of MSN was significantly enhanced, and its BET surface area enlarged to $375.5 \text{ m}^2 \text{ g}^{-1}$. These results demonstrated that TA had been successfully encapsulated into the mesoporous structure of MSN-TA nanocontainers¹¹.

Thereafter, TGA measurements were conducted to quantify the loading ratio of TA in the MSN-TA nanocontainers³⁴. As depicted in Fig. 2c, the TGA curve of TA showed a slight decline from 30 °C to 100 °C, which was caused by water evaporation. A sharp decomposition of TA was observed from 100 °C to 800 °C with a prominent weight loss of 87% (WL_{TA}), which was applied as the temperature range to calculate the loading rate of TA. In this temperature range, the weight loss of MSN (WL_{MSN}) and MSN-TA nanocontainers (WL_{MSN-TA}) was 3.0% and 19.5%, respectively, which means that the weight loss caused by TA decomposition in the MSN-TA nanocontainers was 16.5%. Therefore, the loading rate of TA in the MSN-TA nanocontainers (η_{TA}) can be calculated by the following equation:

$$\eta_{TA} = (WL_{MSN-TA} - WL_{MSN}) / WL_{TA} \times 100\% \quad (1)$$

The η_{TA} was estimated to be 19.0%, representing a relatively high loading efficiency³⁵.

The release behavior of TA from MSN-TA nanocontainers was investigated using ultraviolet-visible (UV-Vis) spectroscopy measurement. Figure 2d presents the UV-Vis spectra of various amounts of TA in 3.5 wt.% NaCl solution. The characteristic absorption peak of TA appeared at 274 nm, which was selected to build the standard UV-Vis curves (shown in the inset of Fig. 2d) and used as the reference to calculate the amount of TA released from the MSN-TA nanocontainers²⁶. Figure 2e depicts the UV-Vis spectra of TA released from the MSN-TA nanocontainers in 3.5

wt.% NaCl solution at different time of immersion. It can be seen that the absorption peak at 274 nm gradually increased, informing the continuous release of TA molecules. The time-dependent release of TA from MSN-TA nanocontainers is plotted in Fig. 2f. TA molecules released rapidly within the first 240 min and then gradually slowed down, finally reaching ~65% after 600 min of release experiment. From the TEM images of MSN-TA nanocontainers (shown in the insets of Fig. 2f), a clear mesoporous structure can be observed after 600 min of release, demonstrating that a large number of TA molecules were released into the saline solution.

Corrosion protection property of EP/MSN-TA coatings

EIS was conducted to explore the influence of MSN-TA addition on the corrosion protection property of coatings. The obtained coatings containing 2.5 wt.%, 5 wt.%, 7.5 wt.% and 10 wt.% of MSN-TA were denoted as EP/MSN-TA_{2.5%}, EP/MSN-TA_{5%}, EP/MSN-TA_{7.5%} and EP/MSN-TA_{10%}, respectively. The Bode impedance modulus plots for the steels covered by different coatings at the initial immersion stage (2 days) are illustrated in Fig. 3a1. All coatings presented a capacitive behavior in the high frequency domain, and a resistive behavior in the low frequency domain. When the immersion time prolonged to 28 days, the resistive response of all coatings occupied a wider frequency domain, indicating a decrease of the barrier property (Fig. 3a2)^{36,37}. Generally, the impedance modulus value at 0.01 Hz ($|Z|_{0.01\text{Hz}}$) can be employed to semi-quantitatively reflect the corrosion protection ability of coatings^{8,9}. As shown in Fig. 3b, the $|Z|_{0.01\text{Hz}}$ values of the blank epoxy, Epoxy/MSN-TA_{2.5%}, Epoxy/MSN-TA_{5%}, Epoxy/MSN-TA_{7.5%}, and Epoxy/MSN-TA_{10%} coatings were respectively $4.6 \times 10^8 \Omega \text{ cm}^2$, $6.0 \times 10^8 \Omega \text{ cm}^2$, $7.1 \times 10^8 \Omega \text{ cm}^2$, $4.4 \times 10^8 \Omega \text{ cm}^2$, and $5.6 \times 10^7 \Omega \text{ cm}^2$ after immersion in 3.5 wt.% NaCl solution for

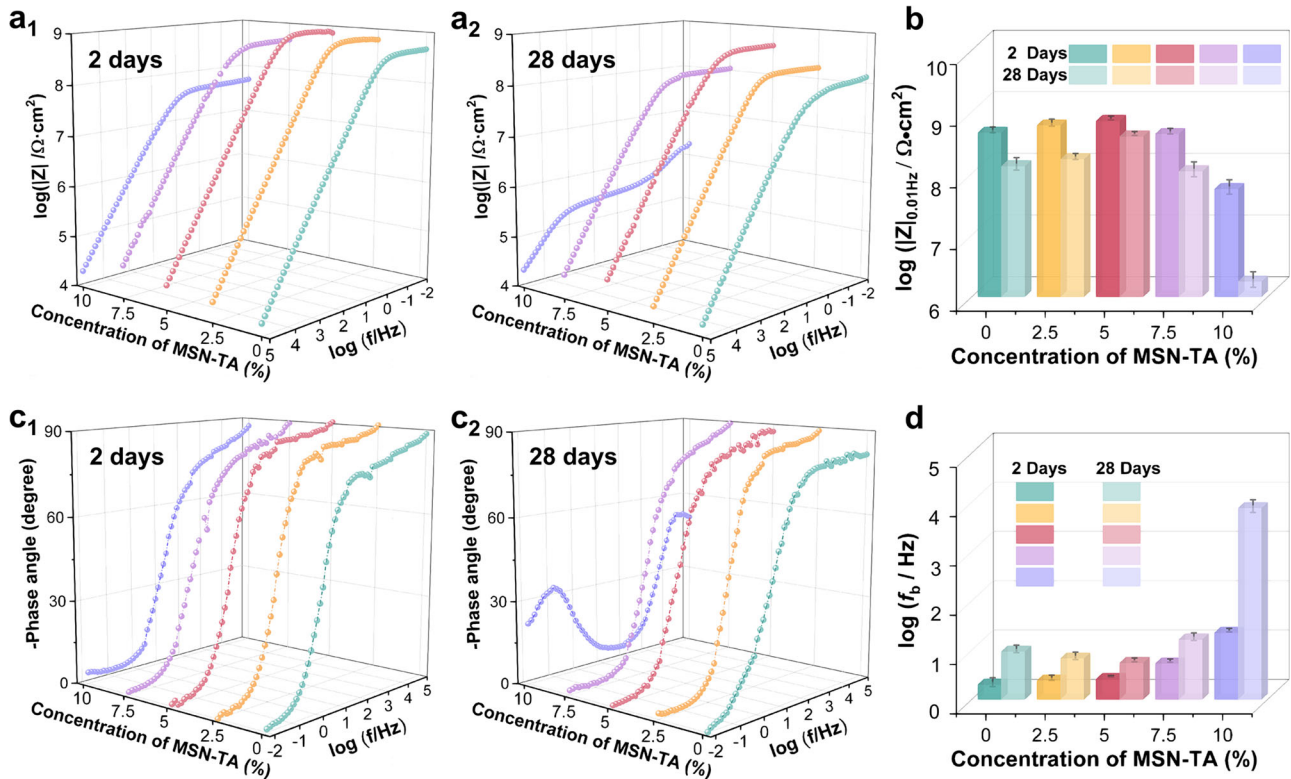


Fig. 3 EIS measurements for intact coatings containing different amounts of MSN-TA nanocontainers. Bode impedance modulus plots of intact epoxy coatings containing different amounts of MSN-TA nanocontainers after (a1) 2 days and (a2) 28 days of immersion in 3.5 wt.% NaCl solution; b the evaluation of $|Z|_{0.01\text{Hz}}$ values for different coatings; Bode phase angle plots of intact epoxy coatings containing different amounts of MSN-TA nanocontainers after (c1) 2 days and (c2) 28 days of immersion in 3.5 wt.% NaCl solution; d the evaluation of f_b values for different coatings (error bars stand for the standard deviations from three independent samples).

2 days. It revealed that the MSN-TA nanocontainers possessed desirable compatibility with the resin when the addition amount of MSN-TA was no >7.5 wt.% in the coating. Further increasing the MSN-TA amount to 10 wt.% caused agglomeration of nanocontainers³⁷, resulting in the generation of detrimental microdefects and thus sharply decreased $|Z|_{0.01\text{Hz}}$ value. After 28 days, the $|Z|_{0.01\text{Hz}}$ values of all coatings declined to some extent. It is worth noting that the Epoxy/MSN-TA_{5%} coating possessed the highest $|Z|_{0.01\text{Hz}}$ value ($4.0 \times 10^8 \Omega \text{ cm}^2$) and the minimum loss of $|Z|_{0.01\text{Hz}}$ values among all the coatings after 28 days of immersion.

Figure 3c1 and c2 display the Bode phase angle plots for the steels protected by different coatings after 2 days and 28 days of immersion in 3.5 wt.% NaCl solution, respectively. The phase angles of the blank epoxy, Epoxy/MSN-TA_{2.5%}, Epoxy/MSN-TA_{5%}, and Epoxy/MSN-TA_{7.5%} coatings presented little change within 28 days. A time constant at the low frequency region was observed for the Epoxy/MSN-TA_{10%} coating after 28 days of immersion, indicating that the aggressive species have reached the steel surface to initiate the corrosion process³⁶. In addition, the breakpoint frequency values (f_b) at -45° from the phase angle plots can determine the deterioration degree of coatings. Larger f_b values usually indicate a higher degree of delamination at the metal/coating interface and worse protective performance of coatings³⁷. The variations of f_b values for different coatings during 28 days of immersion are illustrated in Fig. 3d. It can be seen that the f_b value of the Epoxy/MSN-TA_{10%} coating was the highest after 2 days of immersion and increased sharply after 28 days, indicating the continuous deterioration of the corrosion protection property. In contrast, the elevation of f_b values for the other four coating samples was much slower during the whole immersion period, especially for the Epoxy/MSN-TA_{5%} coating. Therefore, the Epoxy/MSN-TA_{5%} coating with the optimal

corrosion protection performance was applied to determine the weathering resistant, corrosion-warning, and self-healing performances in the following sections.

Weathering resistance of EP/MSN-TA coatings

Before investigating the weathering resistance performance of EP/MSN-TA coatings, the radical scavenging activity of MSN-TA nanocontainers was evaluated via the 1,1-Diphenyl-2-picrylhydrazyl (DPPH) radical scavenging assay³⁸. According to the DPPH colorimetric assays, the color of DPPH will change from dark purple to yellow along with the radical scavenging process, and the UV-Vis absorption spectrum of DPPH at 517 nm will decrease accordingly³⁹. The radical scavenging activity was calculated by the following equation³³:

$$\text{DPPH radical scavenging (\%)} = \left(1 - \frac{A_{\text{sample}} - A_{\text{control}}}{A_0} \right) \times 100\% \quad (2)$$

Where A_{sample} is the absorbance intensity of DPPH solution mixed with the sample solutions containing TA, MSN, or MSN-TA nanocontainers at different concentrations; A_{control} and A_0 are the absorbance intensities of the sample solution and DPPH solution mixed with the same volume of DI water, respectively.

Figure 4a shows the DPPH radical scavenging activity of MSN-TA nanocontainers at different concentrations, using TA molecules and MSN as the control samples. TA molecules showed a significant radical scavenging activity within 30 min of reaction, reaching $\sim 85.9\%$ when the TA concentration was only 4 ppm. Benefiting from the efficient loading of TA in the MSN-TA nanocontainers, MSN-TA also illustrated apparent DPPH radical scavenging activity, which was $\sim 86.1\%$ when the MSN-TA

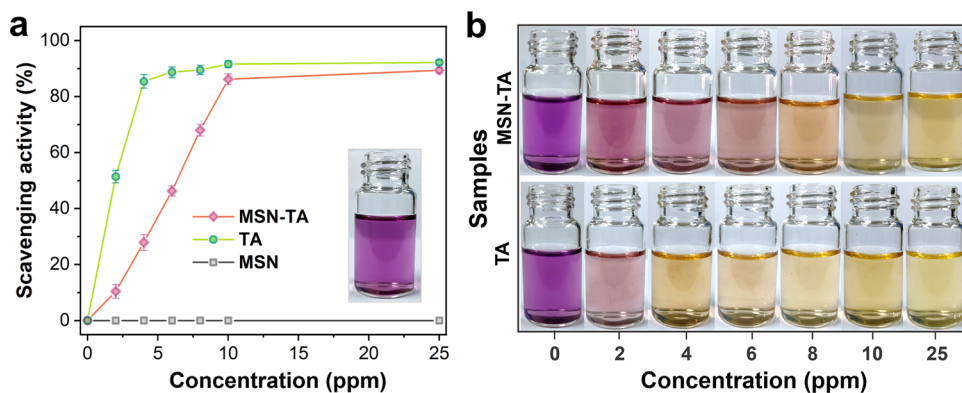


Fig. 4 The DPPH radical scavenging capability of MSN-TA nanocontainers. **a** The DPPH radical scavenging activity of MSN, MSN-TA and TA at different concentrations after 30 min of reaction. The inset is the digital image of DPPH reacted with 25 ppm MSN (error bars stand for the standard deviations from three independent samples); **b** the digital images of DPPH reacted with different concentrations of MSN-TA and TA.

concentration was 10 ppm. In contrast, for the MSN nanocontainers, no radical scavenging activity was shown due to the complete removal of inside TA molecules. Figure 4b shows the digital images of DPPH when reacting with different concentrations of MSN-TA and TA. The color of the mixtures containing MSN-TA nanocontainers and TA molecules turned from dark purple to light purple and finally to yellow color with the increasing of additive concentrations, implying a favorable radical scavenging capability of both MSN-TA and TA.

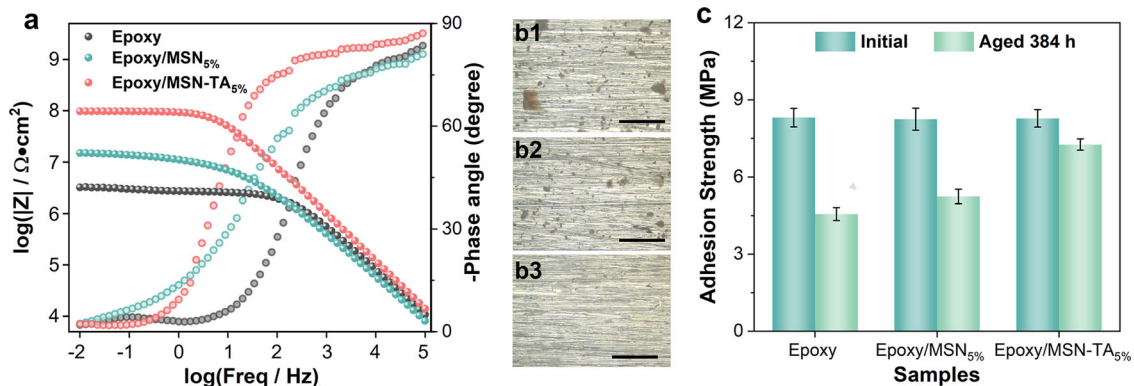
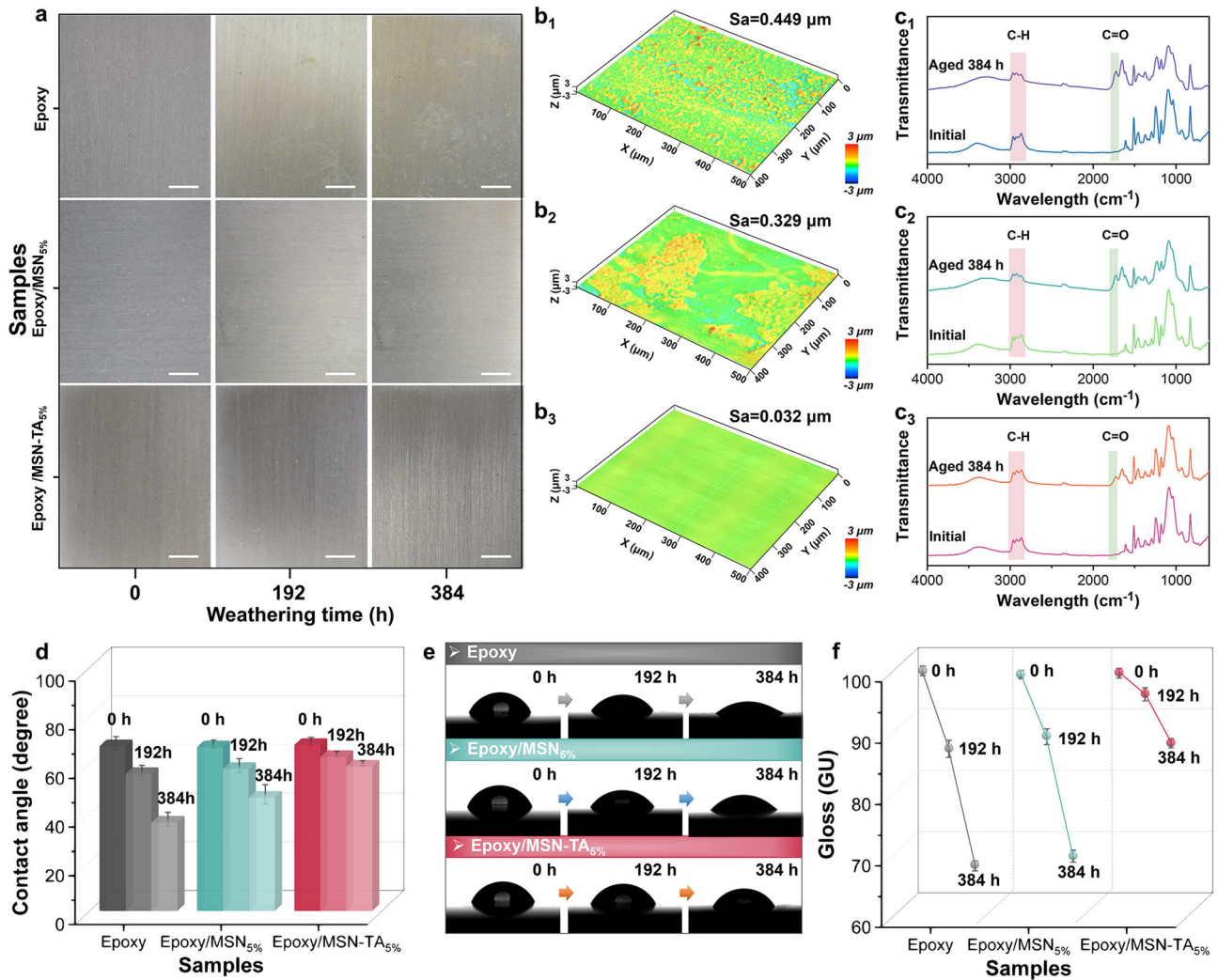
After determining the radical scavenging capability of MSN-TA nanocontainers, accelerated weathering experiments were conducted to evaluate the weathering resistance of EP/MSN-TA_{5%} coating, using the blank epoxy and EP/MSN_{5%} coating (the composite coating containing 5 wt.% MSN without TA) as the control samples. Figure 5a shows the macroscopic images of different coatings before and after accelerated weathering exposure. It can be seen that all the coatings showed a smooth and clean surface morphology before the weathering test. Compared with the blank epoxy and the EP/MSN_{5%} coating, the pristine EP/MSN-TA_{5%} coating illustrated a slight yellowish color as a result of the natural color of TA. With weathering time, some visible white weathering products with hydrophilic and low-molecular chains appeared on the blank epoxy and the EP/MSN_{5%} coating⁴⁰. Moreover, the color of the blank epoxy coating changed into yellow, which can be attributed to the generation of chromophoric groups caused by the degradation of epoxy polymer⁴¹. In contrast, the EP/MSN-TA_{5%} coating exhibited little variation not only in surface morphology but also in coating color appearance.

The typical microscopic morphology and surface roughness (S_a) of different coating surfaces after weathering test were evaluated by confocal laser scanning microscopy (CLSM) analysis⁴². As shown in Fig. 5b1, a rough surface with uniformly distributed bulge was observed on the blank epoxy coating and the S_a value was 0.449 μm , which can be attributed to the generation of weathering products and microscale defects during the degradation of epoxy matrix. As for the EP/MSN_{5%} coating in Fig. 5b2, the weathering products were generated in localized region, and the S_a value (0.329 μm) was a bit lower than that of the blank epoxy. In comparison, the EP/MSN-TA_{5%} coating retained a relatively smooth surface free of weathering products, and the S_a value was as low as 0.032 μm . Moreover, FTIR measurements were performed to study the variation of molecular conformations of different coatings during weathering tests. As illustrated in Fig. 5c1–c3, the difference between the FTIR spectra of the blank epoxy coating, EP/MSN_{5%} coating and EP/MSN-TA_{5%} coating was negligible before the weathering test. After 384 h of accelerated weathering, the characteristic FTIR peaks of the C–H absorption bands ranging from 2820 to 3010 cm^{-1} decreased for all coatings,

indicating that the coatings experienced degradation to some degree⁴³. In addition, a FTIR peak at 1728 cm^{-1} appeared on all coating samples, which was mainly attributed to the C=O group that derived from the oxidation of C–H group in the coating matrix⁴⁴. Among these coatings, the EP/MSN-TA_{5%} coating presented the slightest decline in the peak intensity of C–H bands and the smallest area of the C=O band, implying that the EP/MSN_{5%} coating possessed the highest stability with the least degradation during the weathering test.

The increase of surface roughness and the generation of polar groups can directly influence the surface properties of coatings such as wettability and specular gloss⁴. Water contact angle (WCA) tests were carried out before and after 192 h and 384 h of weathering tests to characterize the evolution of surface wetting property for different coatings. The variation of WCA values and the corresponding images are presented in Fig. 5d, e. Before the weathering test, the blank epoxy, EP/MSN_{5%} and the EP/MSN-TA_{5%} coatings all had average WCA values of 67°, indicating that the addition of nanocantainers had negligible influence on the surface wetting properties of coatings. After weathering tests, the WCA values of all coatings declined gradually, which can be attributed to the generation of hydrophilic groups and the increased surface roughness of the coatings. The WCA values of the blank epoxy coating and the EP/MSN_{5%} coating decreased separately to 36° and 46° after 384 h of weathering exposure, while the EP/MSN-TA_{5%} coating showed the lowest reduction of WCA value (from 67° to 59°), exhibiting a significant weathering resistance. Figure 5f depicts the gloss changes of different coatings during the weathering test. The pristine gloss value of the blank epoxy was 98.8 GU, which decreased significantly to 86.3 GU and 67.2 GU after 192 h and 384 h of weathering exposure, respectively. The gloss decline trend of the EP/MSN_{5%} coating was slightly eased, which could be attributed to the UV light absorbing and scattering ability of MSN⁴⁵. It is worth noticing that the EP/MSN-TA_{5%} coating displayed a much smaller gloss loss, and its gloss value was retained at 87.2 GU after 384 h of weathering exposure. The minimal gloss loss can be ascribed to the dual functions of MSN-TA nanocontainers, with both radical scavenging ability of TA molecules as well as the UV light absorbing and scattering ability of MSN.

The protection property of different coatings after 384 h of weathering test was further evaluated by EIS and pull-off measurements. Figure 6a displays the Bode plots of different coatings after immersion in 3.5 wt.% NaCl solution for 48 h. The $|Z|_{0.01\text{Hz}}$ values of the blank epoxy, the EP/MSN_{5%} and the EP/MSN-TA_{5%} coatings were $3.2 \times 10^6 \Omega \text{cm}^2$, $1.5 \times 10^7 \Omega \text{cm}^2$, and $9.7 \times 10^7 \Omega \text{cm}^2$, respectively. The f_b values of the blank epoxy coating, the EP/MSN_{5%} coating and the EP/MSN-TA_{5%} coating were 235 Hz, 31 Hz, and 8 Hz, respectively. The highest $|Z|_{0.01\text{Hz}}$ and the smallest f_b suggest the best corrosion



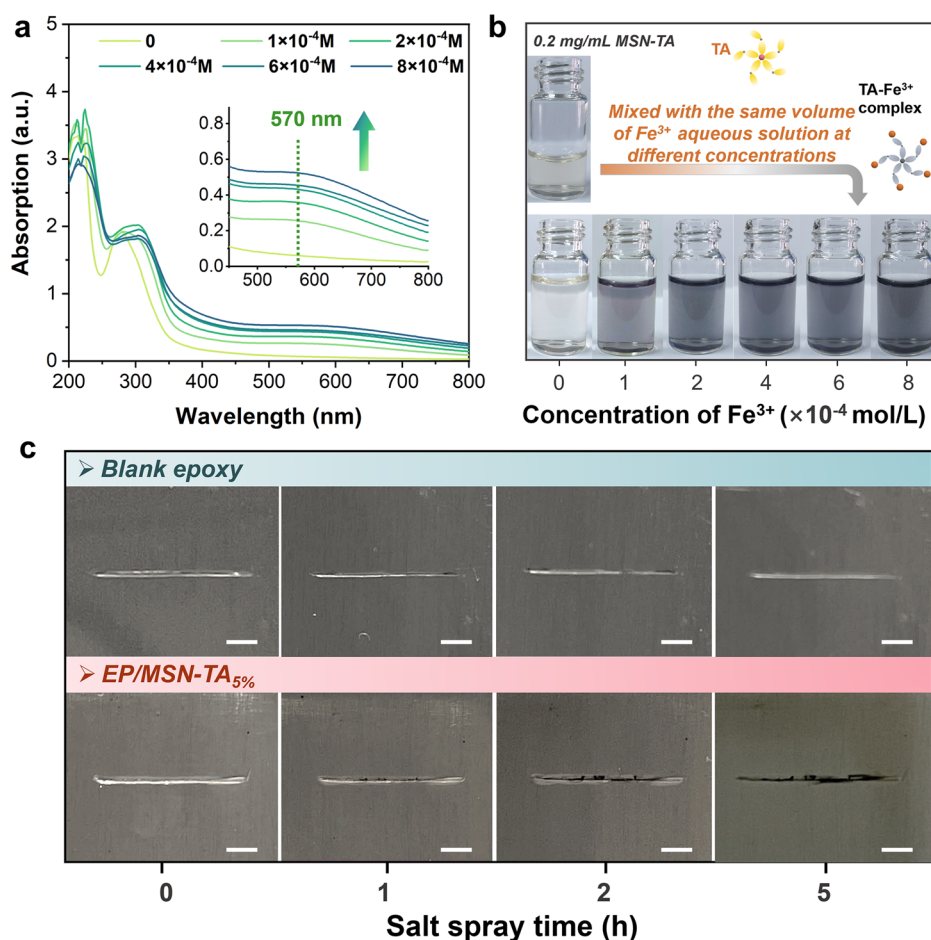


Fig. 7 The coloration response of MSN-TA nanocontainers to Fe^{3+} ions and the corrosion-warning property of EP/MSN-TA_{5%} coating. **a** UV-Vis spectra and **b** optical images of MSN-TA dispersion (0.2 mg mL^{-1}) with the addition of the same volume of Fe^{3+} ion solutions at different concentrations; **c** the optical images of scratches on the surfaces of blank epoxy and the EP/MSN-TA_{5%} coating during salt spray test (scale bar: 1 mm).

protection performance of the EP/MSN-TA_{5%} coating after weathering exposure. Besides, Fig. 6b1–b3 present the optical pictures of the steel surfaces underneath different coatings after 48 h of immersion in 3.5 wt.% NaCl solution. Some corrosion products were found underneath the blank epoxy coating and the EP/MSN_{5%} coating, which can be attributed to the micro-defects generated during the weathering test that accelerated the permeation of corrosive media. In contrast, there was no corrosion product on the steel substrate underneath the EP/MSN-TA_{5%} coating. This can be attributed to two aspects: (1) the radical scavenging ability of TA from MSN-TA nanocontainers can effectively alleviate the degradation of epoxy network during the weathering test; (2) the uniform dispersion of MSN-TA nanocontainers generates a labyrinth effect and forms more tortuous pathways in the coating that inhibit the ingress of corrosive media⁴⁶.

The adhesion strengths of coatings before and after weathering exposure were measured using pull-off measurements. As shown in Fig. 6c, all the coatings showed similar values of the initial adhesion strength ($\sim 8.3 \text{ MPa}$), suggesting that the addition of MSN or MSN-TA nanocontainers did not have a negative effect on the adhesion strength of the epoxy matrix. After 384 h of weathering test, the average adhesion strength values of the blank epoxy, the EP/MSN_{5%} and the EP/MSN-TA_{5%} coatings were 4.5, 5.2, and 7.3 MPa, respectively. The adhesion strength of EP/MSN-TA_{5%} displayed the least reduction, demonstrating that the degradation of epoxy matrix was effectively alleviated⁴⁷.

Corrosion-warning property of EP/MSN-TA coatings

The coloration response of MSN-TA nanocontainers to Fe^{3+} ions was investigated before assessing the corrosion-warning property of EP/MSN-TA coatings. Figure 7a shows the UV-Vis spectra of the mixture solution consisting of 0.2 mg mL^{-1} MSN-TA dispersion and different concentrations of Fe^{3+} ions. After adding Fe^{3+} ions into the MSN-TA dispersion, an obvious absorption peak appeared at 570 nm and the absorption intensity elevated with the increase of Fe^{3+} concentration, indicating the formation of TA/ Fe^{3+} complex²⁶. The corresponding optical images of the MSN-TA dispersion as well as its mixtures with Fe^{3+} ions are displayed in Fig. 7b. The pristine MSN-TA dispersion and its mixture with deionized (DI) water without Fe^{3+} ions were almost colorless. After adding 2 mL of $1 \times 10^{-4} \text{ mol L}^{-1}$ Fe^{3+} aqueous solution into the MSN-TA dispersion, the color of the mixture changed into a light black, which originated from the chelation effect of TA/ Fe^{3+} complex. The black color of the mixture became darker when the concentrations of Fe^{3+} increased from 2×10^{-4} to $8 \times 10^{-4} \text{ mol L}^{-1}$. Due to the prominent black coloration generated from the interaction between TA molecules and Fe^{3+} ions, MSN-TA can serve as a sensitive corrosion indicator providing an early warning of the presence of Fe^{3+} ions during the corrosion initiation on the steel surface.

Thereafter, artificial scratches were made into the blank epoxy and EP/MSN-TA_{5%} coating, and the coatings were exposed to a neutral salt spray environment for 5 h. The corrosion-warning

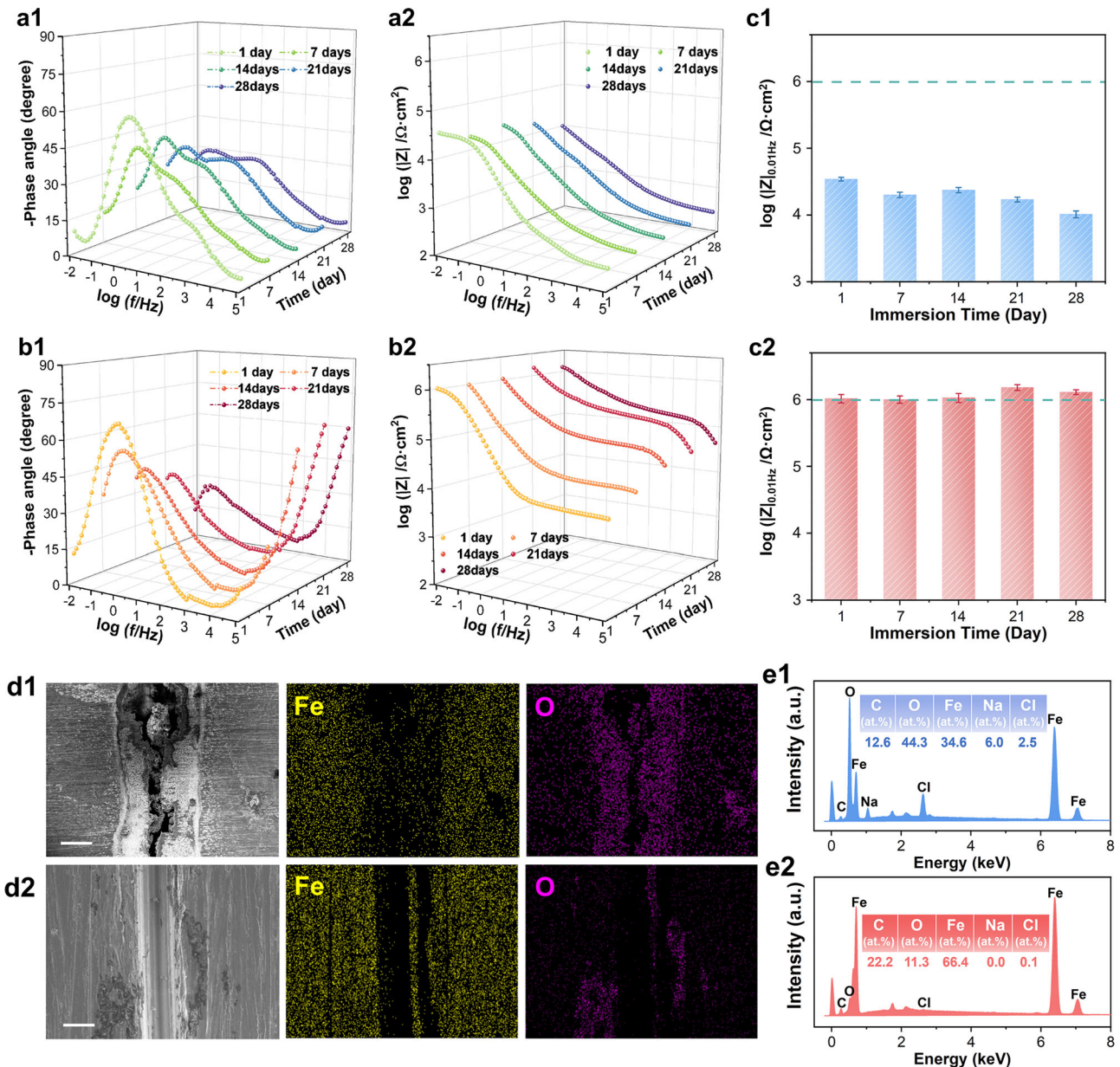


Fig. 8 The self-healing performance of EP/MSN-TA_{5%} coating. Bode plots of (a1–a2) the scratched blank epoxy coating and (b1–b2) the scratched EP/MSN-TA_{5%} coating during immersion in 3.5 wt.% NaCl solution; the variation of $|Z|_{0.01\text{Hz}}$ of (c1) the scratched blank epoxy coating and (c2) the scratched EP/MSN-TA_{5%} coating; SEM images and EDS mapping of the scratches after peeling (d1) the blank epoxy and (d2) the EP/MSN-TA_{5%} coating from the Q235 steel substrates (scale bar: 40 μm); the surface compositions of the Q235 steel substrates at the scratch areas after peeling (e1) the blank epoxy and (e2) the EP/MSN-TA_{5%} coating (error bars stand for the standard deviations from three independent samples).

performance was monitored by recording the color variation along the coating scratches using a digital camera. As shown in Fig. 7c, there was almost no color change near the scratch of the blank epoxy during the whole salt spray test. In contrast, a few scattered black points were observed along the scratch of EP/MSN-TA_{5%} coating within 1 h, and the black coloration was intensified with the salt spray exposure time. After 5 h of spraying, an evident black line was generated along the scratch of the composite coating. Therefore, the EP/MSN-TA_{5%} coating can effectively enable an early corrosion activity warning for the exposed steel surface at a damaged coating area, which is of great significance for timely coating maintenance and structural safety management for industrial applications.

Self-healing property of EP/MSN-TA coatings

The strong chelation effect between TA and Fe³⁺ ions also made it promising for steel corrosion protection by forming a ferric tannate inhibition layer on the steel surface. The corrosion inhibition effect of MSN-TA nanocontainers for carbon steel was demonstrated and discussed in the Supplementary Information. Subsequently, the self-healing process of the scratched EP/MSN-TA_{5%} coating was investigated by EIS measurement, using the blank epoxy coating as the control sample. Figure 8a, b display the Bode plots of different coatings during immersion in 3.5 wt.% NaCl solution for 28 days. The phase angle at high frequency (~10⁵ Hz) can reflect the capacitance behavior of coatings^{48,49}. The EP/MSN-TA_{5%} coating showed much higher phase angle values at the high

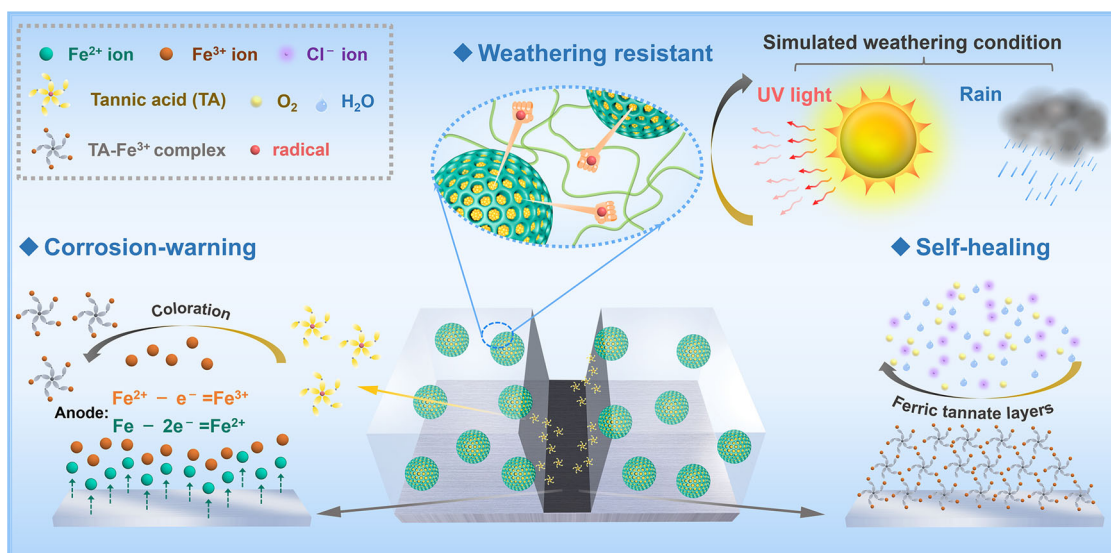


Fig. 9 The schematic illustration of the weathering resistant, corrosion-warning and self-healing functions for the EP/MSN-TA coating.

frequency region than the blank epoxy coating, indicating effective suppression of corrosion activity. In addition, the EP/MSN-TA_{5%} coating showed an obvious increase of the high-frequency phase angles with immersion time, which demonstrated its significant self-healing effect. From the impedance modulus plots, the $|Z|_{0.01\text{Hz}}$ of the scratched blank epoxy coating was $3.5 \times 10^4 \Omega \text{ cm}^2$ at the initial immersion stage (1 day) and decreased gradually to $1.0 \times 10^4 \Omega \text{ cm}^2$ after 28 days. In contrast, the scratched EP/MSN-TA_{5%} coating possessed a relatively high $|Z|_{0.01\text{Hz}}$ value of $1.0 \times 10^5 \Omega \text{ cm}^2$ within 1 day of immersion, and increased slightly to $1.3 \times 10^6 \Omega \text{ cm}^2$ after 28 days. The $|Z|_{0.01\text{Hz}}$ values of the EP/MSN-TA_{5%} coating were two orders of magnitude higher than those of the blank sample during the whole immersion period (see Fig. 8c1 and c2), indicating a substantial self-healing performance of the composite coating.

The surface morphology and elemental composition of the steel substrates at coating damage areas after 28 days of immersion were characterized by SEM and EDS observations. For the substrate covered by the blank epoxy coating (Fig. 8d1), massive corrosion products were generated at the scratch area and resulted in the external expansion. In contrast, the EP/MSN-TA_{5%} coating protected steel displayed few corrosion product near the scratch area (Fig. 8d2). The EDS mapping result of the blank epoxy coated steel surface presented relatively weak Fe element signals and intense O element signals, implying the generation of a significant amount of corrosion products due to the intense corrosion activity at the coating defect area. The EDS mapping of the EP/MSN-TA_{5%} coating showed increased Fe signals and decreased O signals, which indicated that the generation of corrosion products was effectively inhibited. In addition, the EP/MSN-TA_{5%} coating protected steel showed lower Cl levels compared with those for the blank epoxy coating protected steel, indicating that the interaction between chloride ions and metal substrate has been restricted thanks to the surface inhibitive layer⁵⁰. The SEM and EDS mapping results are well aligned with the EIS results, manifesting the effective self-healing performance of the EP/MSN-TA_{5%} coating.

Mechanism of weathering resistant, corrosion-warning and self-healing functions for EP/MSN-TA coating

Figure 9 describes the weathering resistant, corrosion-warning and self-healing functions for the EP/MSN-TA coating. On the one hand, the introduction of MSN-TA nanocontainers can trap the

radicals generated during weathering conditions and scavenge the radicals by donating the hydrogen atoms of o-phenylphenol groups from TA²², which effectively improves the weathering resistance of the epoxy resin. On the other hand, when the coating is damaged, the TA molecules released from the scratched coating will react with the Fe^{3+} ions generated from the corroding steel surface, forming an apparent black chelate product to provide early corrosion warning ability on the corrosion initiation. Simultaneously, the TA/ Fe^{3+} chelate formed over the steel surface can serve as a protective layer to suppress extensive corrosion propagation. Therefore, the introduction of MSN-TA nanocontainers can not only enhance the weathering resistance of epoxy resin, but also endow the coating with timely corrosion-warning and effective self-healing functionalities.

METHODS

Materials

TA (ACS, 98%) was purchased from Alfa Aesar Chemical Co., Ltd. Bisphenol A diglycidyl ether (DGEBA, GC, $\geq 85\%$), TEOS (AR, 99%), neopentyl glycol diglycidyl ether (NGDE, GC, $>40\%$), $\text{FeCl}_3 \cdot 6\text{H}_2\text{O}$ (AR, 99%), and Jeffamine D230 (average Mn ~ 230) were purchased from Aladdin Chemical Co., Ltd. Concentrated ammonium hydroxide (NH_4OH , ACS, 28%), sodium hydroxide (NaOH, AR, 97%), and DPPH (96%) were purchased from Shanghai Macklin Biochemical Co., Ltd. Other reagents and solvents were obtained from Sinopharm Chemical Reagent.

Preparation of MSN-TA nanocontainers

The MSN-TA nanocontainers were prepared by a one-pot method³¹. Typically, 1.1 g TA was thoroughly dissolved in 100 mL ethanol under stirring at 500 r min^{-1} , followed by adding 50 mL NH_4OH . After 1 min of stirring, 0.6 mL TEOS was added into the mixture and stirred for additional 2 h. The MSN-TA nanocontainers were obtained through centrifugation at $10,000 \text{ r min}^{-1}$ for 10 min, washed with DI water twice, and finally freeze-dried for 24 h. For the control experiment, the MSN sample was obtained by calcining the MSN-TA nanocontainers at $500 \text{ }^\circ\text{C}$ for 4 h to completely remove the inside TA molecules.

Preparation of composite coatings

Q235 carbon steel was used as the metal substrate, which was ground with 150 and 240 grit SiC abrasive papers, and then washed thoroughly with ethanol before use. The epoxy coating formulation consisted of two aspects: epoxy resin component and curing agent. Firstly, 1.43 g DGEBA and 0.91 g NGDE were thoroughly mixed as the epoxy resin component, followed by the addition of different weight percentages of the MSN-TA nanocontainers relative to the total weight of polymer matrix (2.5 wt.%, 5 wt.%, 7.5 wt.%, and 10 wt.%). The mixtures were stirred at 500 r min⁻¹ for 4 h to ensure a uniform dispersion of MSN-TA nanocontainers. After that, 0.97 g Jeffamine D230 was added and stirred for an additional 10 min. Thereafter, the obtained mixture was spread over the metal surface using a rod applicator and cured at room temperature for 12 h and then at 55 °C for 24 h¹¹. For the control experiment, the blank epoxy coating without fillers and the composite coating containing 5 wt.% MSN without TA (EP/MSN_{5%}) were similarly prepared. The dry coating thickness for all samples was ~80 μm.

Characterization of MSN-TA nanocontainers

The structure of the MSN-TA nanocontainers was characterized by SEM (G300, ZEISS) and TEM (JEM-2100F, JEOL) equipped with EDS. The chemical components of TA, MSN and MSN-TA nanocontainers were characterized by FTIR (VERTEX 70, Bruker). BET (AUTOSORB IQ, Quantachrome) technique was applied to determine the specific surface area and pore size distribution of MSN-TA nanocontainers based on the nitrogen adsorption-desorption isotherms. To calculate the loading ratio of TA in the MSN-TA nanocontainers, TGA (STA449F5, Netzsch) was conducted during heating from 30 °C to 800 °C under nitrogen atmosphere protection.

The release behavior of TA from MSN-TA in NaCl solution was characterized using a UV-Vis spectrometer (LAMBDA 750, PerkinElmer)¹¹. To begin with, 5 mg MSN-TA was dispersed into 2 mL of 3.5 wt.% NaCl solution and stored in a dialysis bag (MW = 1000), which was then immersed into a beaker containing 48 mL of 3.5 wt.% NaCl solution under stirring at 400 r min⁻¹. After preset time intervals, 3 mL of solution in the beaker was collected and measured using UV-Vis spectroscopy from 200 to 600 nm. After each test, the collected solution was poured back into the beaker and the release test started again. The released amount of TA was calculated based on the obtained UV-Vis spectra and the corresponding standard UV-Vis curves of TA in 3.5 wt.% NaCl solution.

Radical scavenging capacity of MSN-TA nanocontainers

The radical scavenging performance of MSN-TA nanocontainers was assessed by the DPPH radical scavenging activity test^{38,39}, using TA and MSN as control samples. Typically, 2 mL of sample solutions at different concentrations (0, 2, 4, 6, 8, 10, and 25 ppm) were mixed with 2 mL of DPPH solution (0.04 mg mL⁻¹) in ethanol, and then kept in the dark at 25 °C for 30 min. The UV-Vis intensity of the mixture at 517 nm was measured under dim light.

Chelation effect between MSN-TA nanocontainers and Fe³⁺ ions

UV-Vis spectroscopy was used to study the interaction between MSN-TA nanocontainers and Fe³⁺ ions²⁶. To begin with, 0.2 mg mL⁻¹ MSN-TA dispersion and the Fe³⁺ containing aqueous solutions with different concentrations of 1 × 10⁻⁴, 2 × 10⁻⁴, 4 × 10⁻⁴, 6 × 10⁻⁴, and 8 × 10⁻⁴ mol L⁻¹ were pre-prepared. Then 2 mL of the MSN-TA dispersion was mixed with 2 mL of the Fe³⁺ aqueous solutions at different concentrations, and the UV-Vis absorption spectra were measured from 200–800 nm. The optical

images of different mixture solutions were recorded by a digital camera.

Corrosion resistance of the EP/MSN-TA coatings

To evaluate the corrosion resistance property of EP/MSN-TA coatings, the EIS curves of different intact coatings immersed in 3.5 wt.% NaCl solution within 28 days were measured using an electrochemical workstation (PARSTAT 2273, AMETEK). A three-electrode cell was employed, with a platinum sheet as the counter electrode, a saturated calomel electrode (SCE) as the reference electrode, and the coating sample with an exposure area of 1 cm² as the working electrode. EIS data were collected over a 10⁵ Hz to 10⁻² Hz frequency range under a perturbation voltage of 20 mV, and were fitted using the ZSimpwin software^{9,11}.

Weathering resistance of the EP/MSN-TA coatings

The weathering experiment was conducted using an accelerated weathering tester (SUN-II, Shanghai Yiheng Instrument Co., Ltd.). Different coatings were exposed to the UV radiation cycles (300–400 nm, 65 W m⁻²) for 2 h (102 min of irradiation, 18 min of irradiation + simulated spray water), followed by 2 h of dark storage⁵¹. The coating samples were removed from the test cabin for surface characterizations after 192 h and 384 h of accelerated weathering.

The macroscopic morphology evolution of coatings was recorded by a digital camera. The microscopic morphology and roughness of coating surfaces were characterized by CLSM (VK-X, Keyence). FTIR spectra of different coating surfaces before and after 384 h of weathering experiment were tested to evaluate the variation of molecular conformations. The WCAs of different coating surfaces were characterized by the contact angle measurement device (Dataphysics OCA20) with 5 μL water droplets. Gloss measurements were carried out to evaluate the 60° gloss of different coatings according to the GB/T 9574–2007 standard using a WGG60-Y4 glossmeter (KSJ Photoelectrical Instruments Co., Ltd). EIS measurements were conducted on different coatings after 384 h of weathering experiment to assess their weathering resistance property. The corrosion state of metal substrates was observed by CLSM when adjusting observation level to the metal/coating interface. Furthermore, pull-off adhesion test was conducted to evaluate the variation of adhesion strengths of different coatings during 384 h of weathering test. Ergo glue 1690 was applied to glue the aluminum dolly (10 mm in diameter) onto different coating surfaces. The dolly was pulled off by an adhesion tester (PosiTest AT-M) until the coating was detached from the substrate. Each test was performed three times to verify reproducibility and consistency, and to allow statistical analysis of the results.

Corrosion-warning performance of EP/MSN-TA coatings

To demonstrate the corrosion-warning behavior of EP/MSN-TA coatings, through-coating artificial scratches were applied to mimic representative coating damages. The scratches were penetrated through the coating to reach the metal substrate. Salt spray test was carried out on the scratched coatings at 25 °C with a 5 wt.% NaCl solution environment. The color evolution of different coating surfaces was monitored and recorded by a digital camera.

Self-healing performance of EP/MSN-TA coatings

The corrosion inhibition effect of MSN-TA nanocontainers was assessed before evaluating the self-healing performance of coatings. The abraded steel plates were immersed into 3.5 wt.% NaCl solutions in the absence and presence of 2.0 mg mL⁻¹ MSN-TA nanocontainers within 72 h. EIS measurements were carried out to characterize the corrosion inhibition performance of MSN-

TA nanocontainers. After immersion for 72 h, the surface morphology and roughness of steel surfaces were analyzed by CLSM. For analysis of the self-healing performance of EP/MSN-TA coatings, an artificial through-thickness scratch with $\sim 80\ \mu\text{m}$ in width and $\sim 5\ \text{mm}$ in length was made in different coatings using a razor blade, followed by immersing in 3.5 wt.% NaCl solution and carrying out the EIS measurement. All EIS measurements were repeated three times to ensure repeatability. SEM observation and EDS mapping were implemented to reflect the corrosion behavior of steel substrates in coating defect areas.

DATA AVAILABILITY

The data presented in this article is available upon request to the authors.

Received: 20 February 2023; Accepted: 5 May 2023;

Published online: 20 May 2023

REFERENCES

- Williams, G., Kousis, C., McMurray, N. & Keil, P. A mechanistic investigation of corrosion-driven organic coating failure on magnesium and its alloys. *npj Mat. Degrad.* **3**, 41 (2019).
- Larche, J. F., Bussiere, P. O., Therias, S. & Gardette, J. L. Photooxidation of polymers: Relating material properties to chemical changes. *Polym. Degrad. Stabil.* **97**, 25–34 (2012).
- Yan, H., Fan, X., Cai, M., Song, S. & Zhu, M. Amino-functionalized $\text{Ti}_3\text{C}_2\text{T}_x$ loading ZIF-8 nanocontainer@benzotriazole as multifunctional composite filler towards self-healing epoxy coating. *J. Colloid Interf. Sci.* **602**, 131–145 (2021).
- Amrollahi, S., Ramezanzadeh, B., Yari, H., Ramezanzadeh, M. & Mahdavian, M. In-situ growth of ceria nanoparticles on graphene oxide nanoplatelets to be used as a multifunctional (UV shield/radical scavenger/anticorrosive) hybrid compound for exterior coatings. *Prog. Org. Coat.* **136**, 105241 (2019).
- Fernandez-Alvarez, M., Velasco, F. & Bautista, A. Performance of ultraviolet exposed epoxy powder coatings functionalized with silica by hot mixing. *J. Mater. Res. Technol.* **10**, 1042–1057 (2021).
- Motamedi, M., Mohammadkhal, S., Ramezanzadeh, M., Mohammadloo, H. E. & Ramezanzadeh, B. Designing hybrid mesoporous Pr/Tannate-inbuilt ZIF8-decorated MoS_2 as novel nanoreservoirs toward smart pH-triggered anti-corrosion/robust thermomechanical epoxy nanocoatings. *ACS Appl. Mater. Interfaces* **14**, 31170–31193 (2022).
- Saji, V. S. Organic nanotubes for smart anticorrosion and antibiofouling coatings. *npj Mat. Degrad.* **6**, 30 (2022).
- Qian, B. et al. Mussel-inspired self-healing coatings based on polydopamine-coated nanocontainers for corrosion protection. *ACS Appl. Mater. Interfaces* **11**, 10283–10291 (2019).
- Wang, J. et al. Photothermally activated self-healing protective coating based on the “close and seal” dual-action mechanisms. *Compos. Part. B-Eng.* **231**, 109574 (2022).
- Li, C., Guo, X. & Frankel, G. S. Smart coating with dual-pH sensitive, inhibitor-loaded nanofibers for corrosion protection. *npj Mat. Degrad.* **5**, 54 (2021).
- Wang, J. et al. Two birds with one stone: Nanocontainers with synergetic inhibition and corrosion sensing abilities towards intelligent self-healing and self-reporting coating. *Chem. Eng. J.* **433**, 134515 (2022).
- Shkirskiy, V. et al. Cathodic driven coating delamination suppressed by inhibition of cation migration along Zn/polymer interface in atmospheric CO_2 . *npj Mat. Degrad.* **3**, 2 (2019).
- Lu, M. et al. Synthesis of nanoparticle immobilized antioxidants and their antioxidative performances in polymer matrices: a review. *Polym. Int.* **67**, 356–373 (2018).
- Qiu, S. et al. Hindered phenolic antioxidant passivation of black phosphorus affords air stability and free radical quenching. *J. Colloid Interf. Sci.* **606**, 1395–1409 (2022).
- Dintcheva, N. T. & D’Anna, F. Anti-/Pro-oxidant behavior of naturally occurring molecules in polymers and biopolymers: a brief review. *ACS Sustain. Chem. Eng.* **7**, 126565–12670 (2019).
- Xia, W. et al. Functionalized graphene serving as free radical scavenger and corrosion protection in gamma-irradiated epoxy composites. *Carbon* **101**, 315–323 (2016).
- Wu, S., Weng, P., Tang, Z. & Guo, B. Sustainable carbon nanodots with tunable radical scavenging activity for elastomers. *ACS Sustain. Chem. Eng.* **4**, 247–254 (2016).
- Liu, J. et al. Versatile $\text{Ti}_3\text{C}_2\text{T}_x$ MXene for free-radical scavenging. *Nano. Res.* **15**, 2558–2566 (2021).
- Li, Q., Wei, L., Zhang, J., Gu, G. & Guo, Z. Significantly enhanced antioxidant activity of chitosan through chemical modification with coumarins. *Polym. Chem.-Uk.* **10**, 1480–1488 (2019).
- Li, Y. et al. A new strategy to prepare fully bio-based poly(lactic acid) composite with high flame retardancy, UV resistance, and rapid degradation in soil. *Chem. Eng. J.* **428**, 131979 (2022).
- Brito, J. et al. Integrating antioxidant functionality into polymer materials: Fundamentals, strategies, and applications. *ACS Appl. Mater. Interfaces* **13**, 41372–41395 (2021).
- Nimse, S. B. & Pal, D. Free radicals, natural antioxidants, and their reaction mechanisms. *RSC Adv.* **5**, 27986–28006 (2015).
- Peng, Y., Wang, Y., Zhang, R., Wang, W. & Cao, J. Improvement of wood against UV weathering and decay by using plant origin substances: Tannin acid and tung oil. *Ind. Crop. Prod.* **168**, 113606 (2021).
- Qiu, S. et al. A green way to simultaneously enhance the mechanical, flame retardant and anti-ultraviolet aging properties of polylactide composites by the incorporation of tannic acid derivatives. *Polym. Degrad. Stabil.* **196**, 1019831 (2022).
- Ejima, H., Richardson, J. J. & Caruso, F. Metal-phenolic networks as a versatile platform to engineer nanomaterials and biointerfaces. *Nano Today* **12**, 136–148 (2017).
- Liu, C., Qian, B., Hou, P. & Song, Z. Stimulus responsive zeolitic imidazolate framework to achieve corrosion sensing and active protecting in polymeric coatings. *ACS Appl. Mater. Interfaces* **13**, 4429–4441 (2021).
- Qian, B., Hou, B. & Zheng, M. The inhibition effect of tannic acid on mild steel corrosion in seawater wet/dry cyclic conditions. *Corros. Sci.* **72**, 1–9 (2013).
- Xu, W., Han, E. & Wang, Z. Effect of tannic acid on corrosion behavior of carbon steel in NaCl solution. *J. Mater. Sci. Technol.* **35**, 64–75 (2019).
- Wu, Y., Duan, Y., Qiu, J., Gao, X. & Ma, H. A pH-responsive intelligent coating based on composite CaCO_3 microspheres for long-term corrosion protection of Q235 carbon steel. *Appl. Surf. Sci.* **578**, 151980 (2021).
- Li, S. et al. Waterborne polyurethane coating based on tannic acid functionalized Ce-MMT nanocomposites for the corrosion protection of carbon steel. *Prog. Org. Coat.* **163**, 106613 (2022).
- Gao, Z. & Zharov, I. Large pore mesoporous silica nanoparticles by templating with a nonsurfactant molecule, tannic acid. *Chem. Mater.* **26**, 2030–2037 (2014).
- Luo, J. et al. Polyphenols as morphogenetic agents for the controlled synthesis of mesoporous silica nanoparticles. *Chem. Mater.* **31**, 3192–3200 (2019).
- Espina, A., Canameres, M. V., Jurasekova, Z. & Sanchez-Cortes, S. Analysis of iron complexes of tannic acid and other related polyphenols as revealed by spectroscopic techniques: Implications in the identification and characterization of iron gall inks in historical manuscripts. *ACS Omega* **7**, 27937–27949 (2022).
- Wang, J. et al. Corrosion-sensing and self-healing dual-function coating based on 1,10-phenanthroline loaded urea formaldehyde microcapsules for carbon steel protection. *Colloid Surf. A* **652**, 129855 (2022).
- Olivieri, F., Castaldo, R., Cocca, M., Gentile, G. & Lavorgna, M. Mesoporous silica nanoparticles as carriers of active agents for smart anticorrosive organic coatings: a critical review. *Nanoscale* **13**, 9091–9111 (2021).
- Ding, J., Zhao, H. & Yu, H. Bio-inspired multifunctional graphene-epoxy anticorrosion coatings by low-defect engineered graphene. *ACS Nano* **16**, 710–720 (2022).
- Ding, J., Zhao, H. & Yu, H. Structure and performance insights in carbon dots-functionalized MXene-epoxy ultrathin anticorrosion coatings. *Chem. Eng. J.* **430**, 132838 (2021).
- Camargos, C. H. M., Poggi, G., Chelazzi, D., Baglioni, P. & Rezende, C. A. Strategies to mitigate the synergistic effects of moist-heat aging on TEMPO-oxidized nanocellulose. *Polym. Degrad. Stabil.* **200**, 109943 (2022).
- Yi, Z. et al. Preparation of strong antioxidative, therapeutic nanoparticles based on amino acid-induced ultrafast assembly of tea polyphenols. *ACS Appl. Mater. Interfaces* **12**, 33550–33563 (2020).
- Pakravan, H. R. & Yari, H. The influence of nanostructured UV-blockers on mechanical properties of carbon fiber epoxy composites during accelerated weathering condition. *Polym. Advan. Technol.* **29**, 970–981 (2018).
- Nikafshar, S., McCracken, J., Dunne, K. & Nejad, M. Improving UV-Stability of epoxy coating using encapsulated halloysite nanotubes with organic UV-Stabilizers and lignin. *Prog. Org. Coat.* **151**, 105843 (2021).
- Xia, L. et al. Paradox effects of flake carbonyl iron on the photodegradation behaviors of epoxy-based wave-absorbing coatings: Photo-catalytic and UV blocking. *Prog. Org. Coat.* **163**, 106642 (2022).
- An, K. et al. Synergistic reinforcement coating with anti-corrosion and UV aging resistance by filling modified CeO_2 nanoflakes. *Colloid Surf. A* **625**, 126904 (2021).
- Song, S. et al. Multilayer structural epoxy composite coating towards long-term corrosion/wear protection. *Carbon* **183**, 42–52 (2021).
- Amrollahi, S., Mohseni, M. & Ramezanzadeh, B. Fabrication of a low surface energy acrylic/melamine clearcoat with enhanced weathering and biological

- resistances: Investigation of the role of organic UV absorber and nanosilica particles. *Prog. Org. Coat.* **105**, 132–142 (2017).
46. Wang, C. et al. A novel multifunctional coating prepared by internal and external inhomogeneous modification of porous fillers. *Prog. Org. Coat.* **119**, 57–64 (2018).
 47. Ghohrodi, A. R., Ramezanzadeh, M. & Ramezanzadeh, B. Investigating the thermo-mechanical and UV-shielding properties of a nano-porous Zr(IV)-type metal-organic framework (MOF) incorporated epoxy composite coating. *Prog. Org. Coat.* **164**, 106693 (2022).
 48. Tavandashti, N. P. et al. Inhibitor-loaded conducting polymer capsules for active corrosion protection of coating defects. *Corros. Sci.* **112**, 138–149 (2016).
 49. Ma, L. et al. Dual-action self-healing protective coatings with photothermal responsive corrosion inhibitor nanocontainers. *Chem. Eng. J.* **404**, 127118 (2021).
 50. Cheng, L., Liu, C., Wu, H., Zhao, H. & Wang, L. A two-dimensional nanocontainer based on mesoporous polydopamine coated lamellar hydroxyapatite towards anticorrosion reinforcement of waterborne epoxy coatings. *Corros. Sci.* **193**, 109891 (2021).
 51. Yu, F. et al. Preparation and UV aging of nano-SiO₂/fluorinated polyacrylate polyurethane hydrophobic composite coating. *Prog. Org. Coat.* **141**, 105556 (2020).

ACKNOWLEDGEMENTS

This work is supported by the Young Elite Scientists Sponsorship Program by China Association for Science and Technology (YESS, 2020QNRC001), and National Science and Technology Resources Investigation Program of China (Grant No. 2021FY100603).

AUTHOR CONTRIBUTIONS

J.W.: Conceptualization, Methodology, Writing – original draft. W.T.: Investigation, Methodology. H.Y.: Investigation, Methodology. X.R.: Investigation. X.L.: Investigation. L.M.: Supervision, Investigation, Writing – review & editing. C.R.: Investigation. A.M.: Writing – review & editing. D.Z.: Conceptualization, Writing – review & editing.

COMPETING INTERESTS

The author declares no competing interests.

ADDITIONAL INFORMATION

Supplementary information The online version contains supplementary material available at <https://doi.org/10.1038/s41529-023-00360-7>.

Correspondence and requests for materials should be addressed to Lingwei Ma or Dawei Zhang.

Reprints and permission information is available at <http://www.nature.com/reprints>

Publisher's note Springer Nature remains neutral with regard to jurisdictional claims in published maps and institutional affiliations.



Open Access This article is licensed under a Creative Commons Attribution 4.0 International License, which permits use, sharing, adaptation, distribution and reproduction in any medium or format, as long as you give appropriate credit to the original author(s) and the source, provide a link to the Creative Commons license, and indicate if changes were made. The images or other third party material in this article are included in the article's Creative Commons license, unless indicated otherwise in a credit line to the material. If material is not included in the article's Creative Commons license and your intended use is not permitted by statutory regulation or exceeds the permitted use, you will need to obtain permission directly from the copyright holder. To view a copy of this license, visit <http://creativecommons.org/licenses/by/4.0/>.

© The Author(s) 2023